

# Towards optimal point spread function design for resolving point emitters in 3D

JAMES M. JUSUF<sup>1,4</sup> AND MATTHEW D. LEW<sup>1,2,3,\*</sup>

<sup>1</sup>*Department of Electrical and Systems Engineering, Washington University in St. Louis, MO 63130 USA*

<sup>2</sup>*Center for the Science and Engineering of Living Systems, Washington University in St. Louis, MO 63130 USA*

<sup>3</sup>*Institute of Materials Science and Engineering, Washington University in St. Louis, MO 63130 USA*

<sup>4</sup>*Present address: Division of Physics, Mathematics and Astronomy, California Institute of Technology, Pasadena, CA 91125 USA*

\*[mdlew@wustl.edu](mailto:mdlew@wustl.edu)

<https://lewlabs.wustl.edu>

**Abstract:** The past decade has brought many innovations in optical design for 3D super-resolution imaging of point-like emitters, but these methods often focus on single-emitter localization as a performance metric. Here, we propose a simple heuristic for designing a point-spread function (PSF) that allows for precise measurement of the distance between pairs of emitters. We discover that there are two types of PSFs that achieve high performance, as quantified by the Cramér-Rao bound. One is very similar to the existing tetrapod PSF. The other is a rotating, single-spot PSF, which we call the crescent PSF, and it has superior performance for localizing closely spaced emitters throughout a 1- $\mu\text{m}$  focal volume. In addition, it distinguishes between single and two closely spaced emitters with superior accuracy. Our study provides additional insights into optimal strategies for encoding 3D spatial information into optical PSFs.

## 1. Introduction

Recent years have brought significant advances in fluorescence nanoscopy, with three-dimensional (3D) single-molecule (SM) tracking and super-resolution microscopy [1] approaching atomic resolution. A cornerstone of these methods and of the Nobel Prize in Chemistry 2014 [2–4] is the switching of an SM’s emissive state, i.e., experimenter-controlled “blinking,” which enables SMs to be localized independently by minimizing overlap between their individual images, or point-spread functions (PSFs). Over time, these localizations can be stitched together to form a final super-resolved reconstruction. Combined with SM blinking, imaging methods such as interferometry [5–8], fluorescence lifetime imaging near metallic or carbon surfaces [9, 10], and structured illumination with active feedback [11] have all been demonstrated to localize single fluorescent molecules in 3D space with precisions approaching 0.1–1 nm.

However, because the emissive state of any particular fluorophore can only be controlled probabilistically, 3D nanoscopes routinely must detect, resolve, and estimate the positions of emitters whose PSFs overlap on a camera. Methods to improve the resolvability of two emitters laterally separated along the  $x$ - and  $y$ -axes include using PSF engineering for direct imaging [12] and using finite optical structures, such as waveguides, for separating spatial modes in indirect imaging [13]. Additionally, neural networks have achieved impressive performance for the joint task of designing a PSF and resolving dense constellations of emitters within noisy images with high accuracy and resolution [14, 15].

Despite decades of innovation, several outstanding questions remain: 1) How can we express the joint task of resolving and localizing overlapping emitters in 3D mathematically as a performance metric or cost function? Recent advances by Yoav Shechtman and colleagues [14, 15] elegantly adapt a similarity statistic, the Jaccard index, to evaluate if a neural network accurately identifies

and localizes SMs within test images. However, this strategy requires careful design and generation of test data that reflects the imaging task at hand. 2) Given a suitable metric, is there a globally optimal PSF that achieves the best possible performance? Or, are there a few or perhaps many designs that all perform similarly? 3) Finally, are there generalizable design principles that we may interpret as optimal for resolving emitters in 3D? Often, PSF designs resulting from numerical optimization studies are difficult to interpret and generalize. Notably, both rotating PSFs (e.g., the double-helix [16]) and expanding/translating PSFs (e.g., the tetrapod [17]) are widely used for localizing SMs in 3D.

In this theoretical study, we address the questions above by engineering PSFs for resolving pairs of emitters in all three dimensions. We propose a cost function that quantifies a PSF's performance according to its precision in measuring the distance between pairs of emitters with small separation along both the lateral and axial directions, and we apply a gradient descent algorithm to search for PSF(s) that perform optimally. Surprisingly, regardless of the initial condition, all runs of the algorithm converged to one of two designs. The first is a single-“spot” PSF that rotates as a function of emitter depth, which we call the crescent PSF, and the second is a double-spot PSF that mimics the existing Tetrapod PSFs by expanding laterally as a function of emitter depth. We quantify the theoretical performance of these PSFs by calculating the classical Cramér-Rao bounds (CRBs) for estimating positional quantities in one- and two-emitter configurations. Moreover, a likelihood-ratio test on simulated data demonstrates that compared to other engineered PSFs, the crescent PSF allows for distinguishing between one emitter and two axially separated emitters with superior accuracy.

## 2. Designing imaging systems for resolving closely spaced emitter pairs in three dimensions

### 2.1. Mathematical framework

We frame our study on resolving emitters in 3D as a PSF design problem. To express the PSF of a microscope mathematically, we begin by considering a single ideal point emitter located at  $(x_0, y_0, z_0)$  in object space, which produces the following classical wave function in the Fourier plane of the microscope:

$$\psi(x_F, y_F; x_0, y_0, z_0) = A \left(1 - r_F^2\right)^{-1/4} \text{circ}\left(\frac{nr_F}{\text{NA}}\right) \exp\left[\frac{i2\pi n}{\lambda_0} \left(x_0 x_F + y_0 y_F + z_0 \sqrt{1 - r_F^2}\right)\right]. \quad (1)$$

Here,  $x_F$  and  $y_F$  are the spatial coordinates in the Fourier plane,  $n$  is the index of refraction of the medium surrounding the emitter,  $\text{NA}$  is the numerical aperture of the microscope,  $\lambda_0$  is the free-space wavelength of the emitter, and  $r_F = \sqrt{x_F^2 + y_F^2}$ . The circular aperture function  $\text{circ}$  denotes the disk-shaped support of the wavefunction in Fourier space and is defined as

$$\text{circ}(\rho) = \begin{cases} 1 & \rho \leq 1 \\ 0 & \text{otherwise,} \end{cases} \quad (2)$$

and the normalization factor  $A$  is given by

$$A = \left[2\pi \left(1 - \sqrt{1 - (\text{NA}/n)^2}\right)\right]^{-1/2}, \quad (3)$$

ensuring that  $\iint dx_F dy_F |\psi(x_F, y_F; x_0, y_0, z_0)|^2 = 1$ . A phase mask (PM) in the Fourier plane, described by a function  $\varphi_{\text{mask}}(x_F, y_F)$  with range  $[-\pi, \pi]$ , modifies the wave function and enables us to design the image of the emitter with high photon efficiency (Figure 1A). The final PSF is given by

$$I(x_I, y_I; x_0, y_0, z_0) = |\mathcal{F}\{\psi(x_F, y_F; x_0, y_0, z_0) \exp[i\varphi_{\text{mask}}(x_F, y_F)]\}|^2, \quad (4)$$

where  $\mathcal{F}$  is a two-dimensional Fourier transform.

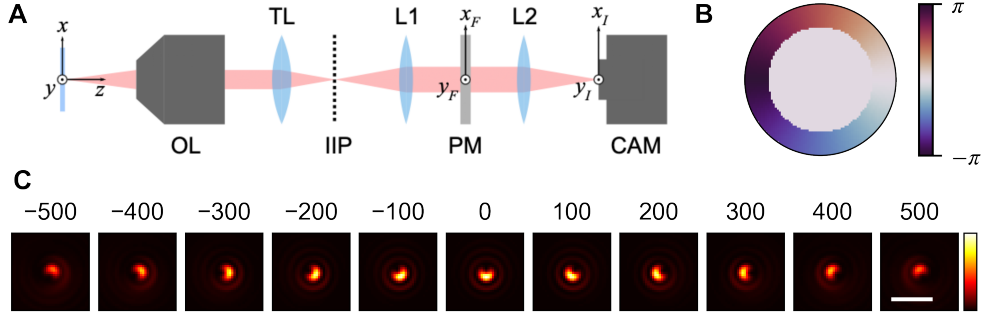


Fig. 1. Microscope and 4f system for implementing the crescent PSF. (A) A 4f system comprising two lenses (L1, L2,  $f = 150$  mm) and a phase mask (PM) is attached to a standard microscope with an objective lens (OL) and tube lens (TL,  $f = 200$  mm). The intermediate image plane (IIP) and camera (CAM) image planes are conjugate to the focal plane of OL. The coordinates  $x_F$  and  $y_F$  are scaled such that the aperture has radius  $\text{NA}/n$ . (B) The optimized phase mask that produces the crescent PSF. The colorbar represents phase in radians. (C) Images of the optimized crescent PSF as a function of emitter depth in nm. The color scale is in arbitrary units of intensity. Scale bar = 1  $\mu\text{m}$ .

In SM imaging, the probabilistic nature of photon detection must be considered. Estimating the positions of emitters from noisy images is appropriately viewed as a statistical parameter estimation problem. Given a quantity of interest  $\theta$ , which could be an emitter's  $x$ -coordinate, for instance, the Cramér-Rao bound (CRB) provides a lower bound on the variance of any unbiased estimator  $\hat{\theta}$  of  $\theta$ :

$$\text{Var}(\hat{\theta}) \geq \left( \sigma_{\theta}^{(\text{CRB})} \right)^2. \quad (5)$$

Therefore,  $\sigma_{\theta}^{(\text{CRB})}$  can be used to quantify the precision with which a given optical system can measure  $\theta$ . It is related to the Fisher information  $F(\theta)$  by

$$\left( \sigma_{\theta}^{(\text{CRB})} \right)^2 = [F(\theta)]^{-1}. \quad (6)$$

For an image containing  $N_{\text{sig}}$  signal photons collected from the emitter and a constant background flux of  $N_{\text{bg}}$  photons per pixel, Poisson statistics of photon detection dictate that the Fisher information is given by

$$F(\theta) = \iint dx_I dy_I \frac{N_{\text{sig}}^2}{N_{\text{sig}} p(x_I, y_I | \theta) + N_{\text{bg}}} \left[ \frac{\partial}{\partial \theta} p(x_I, y_I | \theta) \right]^2, \quad (7)$$

where  $p(x_I, y_I | \theta)$  represents the probability density of photon detection over image space. For a single point emitter, this is equivalent to the PSF, given in Equation (4):

$$p(x_I, y_I | x_0, y_0, z_0) = I(x_I, y_I; x_0, y_0, z_0). \quad (8)$$

The formalism above can be extended for the case of two incoherent emitters. For two equally bright point emitters located at  $(x_c \pm \Delta x/2, y_c, z_c)$ , where the subscript  $c$  is used to denote their “centroid” position, the probability density becomes

$$p(x_I, y_I | x_c, \Delta x, y_c, z_c) = \frac{1}{2} [I(x_I, y_I; x_c + \Delta x/2, y_c, z_c) + I(x_I, y_I; x_c - \Delta x/2, y_c, z_c)]. \quad (9)$$

If  $\Delta x$  is sufficiently small, then  $I(x_I, y_I; x_c \pm \Delta x/2, y_c, z_c)$  can be expanded as a Taylor series along the separation direction:

$$p(x_I, y_I | x_c, \Delta x, y_c, z_c) = I(x_I, y_I; x_c, y_c, z_c) + \frac{\Delta x^2}{8} \frac{\partial}{\partial x} I(x_I, y_I; x, y_c, z_c) |_{x=x_c} + \dots \quad (10)$$

By substituting Equation (10) into Equation (7), we obtain the Fisher information  $F(\Delta x)$  and corresponding precision  $\sigma_{\Delta x}^{(\text{CRB})}$  for estimating  $\Delta x$ . Defining the following quantity,

$$S_x \equiv \iint dx_I dy_I \frac{N_{\text{sig}}^2}{N_{\text{sig}} I(x_I, y_I; x_c, y_c, z_c) + N_{\text{bg}}} \left[ \frac{\partial}{\partial x} I(x_I, y_I; x, y_c, z_c) |_{x=x_c} \right]^2, \quad (11)$$

for sufficiently small  $\Delta x$  the Fisher information is  $F(\Delta x) \approx \Delta x^2 S_x / 16$ , and the estimation precision is

$$\sigma_{\Delta x}^{(\text{CRB})} \approx \frac{4}{\Delta x \sqrt{S_x}}. \quad (12)$$

Analogous statements can be made for two emitters separated along the  $y$ - and  $z$ -axes. For two emitters located at  $(x_c, y_c \pm \Delta y, z_c)$ , define

$$S_y \equiv \iint dx_I dy_I \frac{N_{\text{sig}}^2}{N_{\text{sig}} I(x_I, y_I; x_c, y_c, z_c) + N_{\text{bg}}} \left[ \frac{\partial}{\partial y} I(x_I, y_I; x_c, y, z_c) |_{y=y_c} \right]^2, \quad (13)$$

and the estimation precision for  $\Delta y$  is

$$\sigma_{\Delta y}^{(\text{CRB})} \approx \frac{4}{\Delta y \sqrt{S_y}}. \quad (14)$$

Similarly, for two emitters located at  $(x_c, y_c, z_c \pm \Delta z)$ , define

$$S_z \equiv \iint dx_I dy_I \frac{N_{\text{sig}}^2}{N_{\text{sig}} I(x_I, y_I; x_c, y_c, z_c) + N_{\text{bg}}} \left[ \frac{\partial}{\partial z} I(x_I, y_I; x_c, y_c, z) |_{z=z_c} \right]^2, \quad (15)$$

and the estimation precision for  $\Delta z$  is

$$\sigma_{\Delta z}^{(\text{CRB})} \approx \frac{4}{\Delta z \sqrt{S_z}}. \quad (16)$$

A comparison of the approximations in Equations (12), (14) and (16) against their true values is shown in Appendix A, Figure 5.

## 2.2. Gradient descent optimization

In order to engineer a PSF that excels at resolving closely spaced pairs of emitters in 3D, rather than simply localizing single emitters, we wish to find a PM that simultaneously minimizes  $\sigma_{\Delta x}^{(\text{CRB})}$ ,  $\sigma_{\Delta y}^{(\text{CRB})}$ , and  $\sigma_{\Delta z}^{(\text{CRB})}$  for two equally bright, incoherent point emitters in various spatial configurations. One approach is to find a PM that minimizes the following cost function:

$$C_0 = \left( \sigma_{\Delta x}^{(\text{CRB})} \right)^2 + \left( \sigma_{\Delta y}^{(\text{CRB})} \right)^2 + \left( \sigma_{\Delta z}^{(\text{CRB})} \right)^2. \quad (17)$$

It is worth noting that  $\sigma_{\Delta x}^{(\text{CRB})}$  is well-defined for any placement of two emitters, including one with a nonzero  $y$ - and  $z$ - separation. However, to reduce the computational complexity of the problem, we calculate  $\sigma_{\Delta x}^{(\text{CRB})}$  for emitters separated along the  $x$ -axis only (Equations (11) and (12)).

Similarly, we calculate  $\sigma_{\Delta y}^{(\text{CRB})}$  for emitters with  $y$ -separation only (Equations (13) and (14)) and  $\sigma_{\Delta z}^{(\text{CRB})}$  for emitters with  $z$ -separation only (Equations (15) and (16)). This convention is used throughout the remainder of the paper.

In addition to the PM,  $C_0$  also depends on a multitude of variables, namely  $x_c$ ,  $y_c$ ,  $z_c$ ,  $\Delta x$ ,  $\Delta y$ ,  $\Delta z$ ,  $N_{\text{sig}}$ , and  $N_{\text{bg}}$ . The engineered PSF should minimize  $C_0$  over a reasonable domain of these parameters. Since the optical system is shift-invariant, and the integrals in Equations (11), (13) and (15) are evaluated over the entire image space, all  $\sigma^{(\text{CRB})}$  are independent of  $x_c$  and  $y_c$ . We therefore fix  $x_c = y_c = 0$  without loss of generality. We also set  $N_{\text{sig}} = 1000$  and  $N_{\text{bg}} = 10$ , which reflect typical SM imaging experiments. Furthermore, the Taylor expansion has decoupled the dependence of  $\sigma_{\Delta x}^{(\text{CRB})}$  on the PM from its dependence on  $\Delta x$ , and the same argument applies for  $\sigma_{\Delta y}^{(\text{CRB})}$  and  $\sigma_{\Delta z}^{(\text{CRB})}$ ; it therefore suffices to minimize

$$C_1 = \frac{1}{S_x} + \frac{1}{S_y} + \frac{1}{S_z}, \quad (18)$$

which now only depends on the PM and  $z_c$ .

To find a PM  $\varphi_{\text{mask}}$  that minimizes  $C_1$  over a range of  $z_c$ , we apply a gradient descent optimization algorithm. The algorithm seeks to minimize a cost function  $C_2$ , which we define to be proportional to the mean value of  $C_1$  over 15 equally-spaced values of  $z_c$  between  $-500$  nm and  $500$  nm:

$$C_2(\varphi_{\text{mask}}) = \frac{\beta}{15} \times \sum_{z_c \in \{-500 \text{ nm}, \dots, 500 \text{ nm}\}} C_1(\varphi_{\text{mask}}, z_c). \quad (19)$$

The constant  $\beta$  can be chosen freely to scale the values of  $C_2$  to any desired order of magnitude.

To carry out the computations, the continuous function  $\varphi_{\text{mask}}$  is parametrized as a real-valued  $256 \times 256$  matrix whose elements represent a discretely-sampled (i.e., pixelated) phase mask. A pseudocode version of the gradient descent algorithm is shown below in Algorithm 1.

---

**Algorithm 1:** Gradient descent for designing phase mask  $\varphi_{\text{mask}}$  to minimize cost function  $C_2$  (Equation (19))

---

```

i ← 0;                                /*  $i_{\text{max}}$  sets the number of iterations */
while  $i < i_{\text{max}}$  do
     $\mathbf{v} \leftarrow \mathbf{v} - \alpha \nabla_{\mathbf{v}} C_2(\varphi_{\text{mask}}, \mathbf{v})$ ; /*  $\mathbf{v}$  is a vector of PM pixels,  $\alpha$  is
    a user-defined learning rate,  $\varphi_{\text{mask}, \mathbf{v}}$  is the phase
    mask parametrized by  $\mathbf{v}$  */
     $i \leftarrow i + 1$ ;
end
return  $\mathbf{v}$ ;

```

---

We use the Python programming language (version 3.7.11) and TensorFlow machine learning library (version 2.0.0) to implement the algorithm. All PSFs are calculated for an imaging system with  $\text{NA} = 1.4$ ,  $n = 1.518$ , and  $\lambda_0 = 550$  nm, which corresponds to a PM pixel size of  $d_{\text{PM}} = 49.58$   $\mu\text{m}$  and an image pixel size of  $d_I = 58.5$  nm when calculating the PSF using a 2D discrete Fourier transform. These values are chosen to reflect a typical laboratory setup and are used to generate all the results in this paper. The nonzero values of the PM matrix are restricted to a centered disk of radius 38.12 px, representing the aperture of the microscope's objective lens. We also set  $\beta = 1.6 \times 10^{29}$  in Equation (19) such that when distances are inputted in meters, typical values of  $C_2$  are on the order of 10.

Since there is no reason to assume that  $C_2$  is a convex function of the PM's pixel values, the local minimum to which gradient descent converges may depend on the initial condition. Thus,

the algorithm is run from 11 different initial PMs (Figure 2 and Appendix A, Figure 6). Four of the initial PMs correspond to existing PSFs engineered for 3D localization of single emitters: these are the corkscrew [18], double helix [16], and two PSFs from the Tetrapod family [17], termed tetra2 and tetra3 in this paper. Another PM is a random array, i.e., each pixel value is sampled independently from  $\text{Uniform}(-\pi, \pi)$ . The six remaining PMs are generated by adding the 63 Zernike polynomials with  $2 \leq n \leq 10$  with coefficients sampled independently from  $\text{Normal}(0, \sigma = 0.05)$ . The first three Zernike polynomials ( $n = 0, 1$ ) are excluded since they do not affect  $C_2$ . The learning rate  $\alpha$  is set to 25 for the corkscrew, double helix, tetra2, and tetra3 initial conditions, 1 for the random pixels initial condition, and 10 for the random Zernike initial conditions. The algorithm is run for a total of 600 iterations, which is sufficient for all runs to converge (Appendix A, Figure 7).

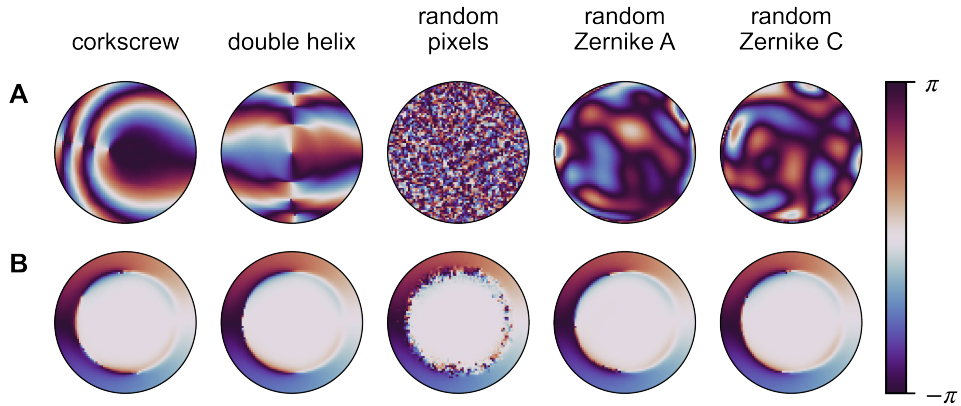


Fig. 2. Optimality and stability of the crescent PSF. (A) The various initial PMs, including those of the corkscrew [18] and double helix [16], that converge to the crescent PM when optimized by Algorithm 1. (B) The final PMs, normalized as described in Appendix A, Figure 8. The PSFs generated by the final PMs are virtually indistinguishable from the PSF in Figure 1c and are therefore not shown. The colorbar represents phase in radians.

The final PMs are normalized such that their PSFs are centered laterally in the image plane and similar PSFs share the same orientation (Appendix A, Figure 8). It is then evident that the PMs fall into two categories. Five PMs consist of a ring-shaped ramp around a circular region of constant zero phase (Figure 2). The results are essentially identical except for minor imperfections at the boundary between the two regions. We therefore designed an idealized version of the PM (Figure 1b and Appendix A, Figure 9). This PM produces a single-spot PSF that rotates as a function of emitter depth (Figure 1c), which we call the crescent PSF. Its rotation and shape bear a striking resemblance to the corkscrew PSF [18, 19], even though its PM is remarkably different. The remaining six final PMs produce a PSF that resembles the existing Tetrapod (Appendix A, Figure 6).

### 3. Precision of crescent PSF for one- and two-emitter localization

To compare the performance of the crescent PSF with existing engineered PSFs, we calculate  $\sigma^{(\text{CRB})}$  for estimating various positional quantities within a 1- $\mu\text{m}$  depth range ( $-500 \text{ nm} \leq z_c \leq 500 \text{ nm}$ ) in the cases of imaging both one and two emitters (Figure 3).

In the one-emitter case (Figure 3A), the emitter is located at  $(x_0, y_0, z_0)$ , and  $\sigma_x^{(\text{CRB})}$  and  $\sigma_z^{(\text{CRB})}$  are the precisions of estimating  $x_0$  and  $z_0$  respectively from the noisy image. It should be

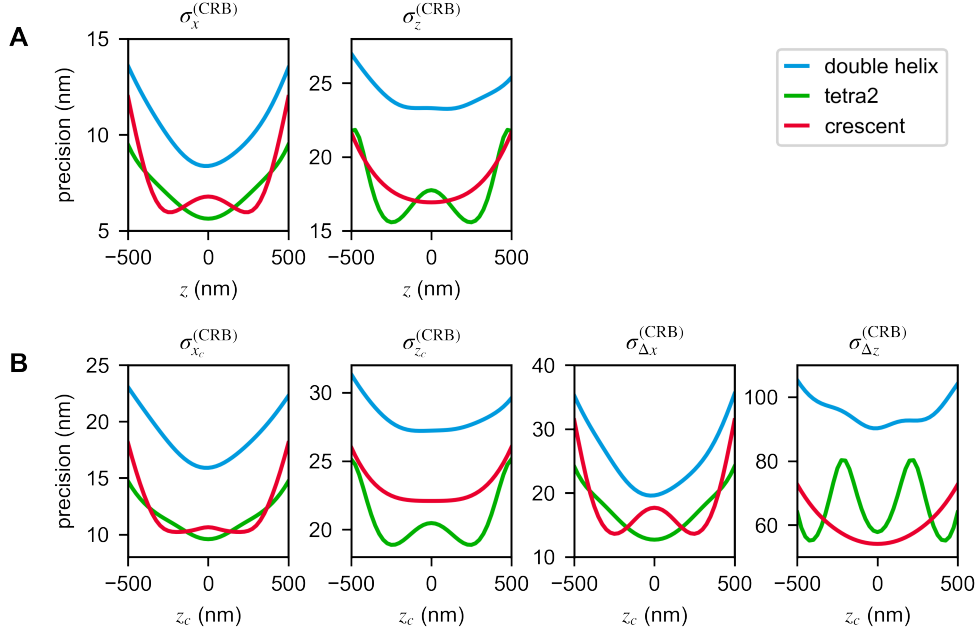


Fig. 3. Localization precision of the double-helix (cyan), tetrapod (green), and crescent (red) PSFs for imaging a single isolated emitter at axial position  $z$  and (B) two closely spaced emitters centered at axial position  $z_c$ . For the two-emitter cases, the precision of calculating lateral centroid  $\sigma_{x_c}^{(\text{CRB})}$ , axial centroid  $\sigma_{z_c}^{(\text{CRB})}$ , lateral separation  $\sigma_{\Delta x}^{(\text{CRB})}$ , and axial separation  $\sigma_{\Delta z}^{(\text{CRB})}$  are shown. The precisions are calculated for emitters that are separated laterally ( $\sigma_x^{(\text{CRB})}$  and  $\sigma_{\Delta x}^{(\text{CRB})}$ ) or axially ( $\sigma_z^{(\text{CRB})}$  and  $\sigma_{\Delta z}^{(\text{CRB})}$ ) by 200 nm. Due to symmetry,  $\sigma_y^{(\text{CRB})} = \sigma_x^{(\text{CRB})}$  and  $\sigma_{\Delta y}^{(\text{CRB})} = \sigma_{\Delta x}^{(\text{CRB})}$ . In all cases,  $N_{\text{sig}} = 1000$  photons and  $N_{\text{bg}} = 10$  photons per pixel.

noted that in previous sections, Fisher information and CRBs were defined for single-parameter estimation only, whereas now we calculate CRBs for multi-parameter estimation, using the  $3 \times 3$  Fisher information matrix for parameters  $x_0$ ,  $y_0$ , and  $z_0$  [20]. This more accurately reflects the practical scenario where one needs to simultaneously estimate  $x_0$ ,  $y_0$  and  $z_0$ , and the CRBs may be affected by covariances between the parameters.

In the two-emitter case (Figure 3B), we consider both laterally and axially separated emitters. For laterally separated emitters at  $(x_c \pm 100 \text{ nm}, y_c, z_c)$ , we calculate  $\sigma_{x_c}^{(\text{CRB})}$ , the precision of estimating the  $x$ -coordinate of the centroid  $x_c$ , as well as  $\sigma_{\Delta x}^{(\text{CRB})}$ . For axially separated emitters at  $(x_c, y_c, z_c \pm 100 \text{ nm})$ , we calculate  $\sigma_{z_c}^{(\text{CRB})}$  and  $\sigma_{\Delta z}^{(\text{CRB})}$ . Note that the plotted values of  $\sigma_{\Delta x}^{(\text{CRB})}$  and  $\sigma_{\Delta z}^{(\text{CRB})}$  are exact values, unlike the approximations in Equations (12) and (16). Furthermore, the centroid estimation CRBs are calculated using the Fisher information matrix for parameters  $x_c$ ,  $y_c$ , and  $z_c$ , and the separation estimation CRBs are calculated using the Fisher information matrix for  $\Delta x$ ,  $\Delta y$ , and  $\Delta z$ . The separation of 200 nm is chosen specifically so that the two emitters would be difficult but not impossible to resolve. For reference, a standard microscope with the same parameters has an Abbe diffraction limit of  $\lambda_0/2\text{NA} = 196 \text{ nm}$ . In all cases, we assume that a total of 1000 photons are detected from the emitters with a total background flux of 10 photons per pixel.

Interestingly, the double-helix and tetra2 PSFs, which are optimized for localizing single

emitters in 3D, do not perform optimally for resolving two closely separated emitters in 3D ( $\sigma_{\Delta z}^{(\text{CRB})} = 95.4 \pm 4.1$  nm for double helix,  $\sigma_{\Delta z}^{(\text{CRB})} = 65.5 \pm 8.4$  nm for tetra2, mean $\pm$ std over a depth range of 1  $\mu\text{m}$ ). The performance of the new Tetrapod-like PSF produced by gradient descent is very similar to that of the existing tetra2 PSF (Appendix A, Figure 10).

The crescent PSF is superior for estimating the separation between emitters ( $\sigma_{\Delta x}^{(\text{CRB})} = 18.0 \pm 4.9$  nm,  $\sigma_{\Delta z}^{(\text{CRB})} = 60.2 \pm 5.7$  nm) without compromising performance in localizing single emitters. There is a slight degradation in the crescent PSF's performance for localizing the centroid along the axial direction ( $\sigma_{z_c}^{(\text{CRB})} = 23.1 \pm 1.2$  nm, 11% worse than tetra2), but this tradeoff comes with the benefit of decreased variability and 8% superior performance for estimating emitter separation along the  $z$  direction.

#### 4. Accuracy of crescent PSF in distinguishing between one and two emitters

To further investigate the ability of the crescent PSF to resolve emitters with small separation in the axial direction, we test its performance in distinguishing between noisy images of one vs. two emitters. We consider emitters with  $\Delta z = 100$  nm and  $N_{\text{sig}} = 10000$  photons,  $\Delta z = 200$  nm and  $N_{\text{sig}} = 2000$  photons, and  $\Delta z = 400$  nm and  $N_{\text{sig}} = 1000$  photons, all with  $N_{\text{bg}} = 10$  photons per pixel. For each configuration, we vary  $z_c$  from  $-500$  nm to  $500$  nm and test four different PSFs. For each data point, we simulate 10000 noisy images of two emitters at  $(0, 0, z_c \pm \Delta z/2)$ , and for each image, a likelihood-ratio test is used to distinguish between two emitters versus the null hypothesis of one emitter at  $(0, 0, z_c)$ . Denoting the photon counts in the noisy image by  $I_N(x_I, y_I)$ , and assuming a Poisson-distributed photon counting process, the likelihoods of the two scenarios are defined as follows:

$$\begin{aligned} \mathcal{L}(1 \text{ emitter}) &= P(I_N | 1 \text{ emitter}) \\ &= \sum_{(x_I, y_I)} \frac{[N_{\text{sig}} I(x_I, y_I; x_0, y_0, z_0) + N_{\text{bg}}]^{I_N(x_I, y_I)}}{\exp[N_{\text{sig}} I(x_I, y_I; x_0, y_0, z_0) + N_{\text{bg}}] [I_N(x_I, y_I)]!} \end{aligned} \quad (20)$$

$$\begin{aligned} \mathcal{L}(2 \text{ emitters}) &= P(I_N | 2 \text{ emitters}) \\ &= \sum_{(x_I, y_I)} \frac{\{N_{\text{sig}} [I(x_I, y_I; x_c, y_c, z_c + \frac{\Delta z}{2}) + I(x_I, y_I; x_c, y_c, z_c - \frac{\Delta z}{2})] + N_{\text{bg}}\}^{I_N(x_I, y_I)}}{\exp \{N_{\text{sig}} [I(x_I, y_I; x_c, y_c, z_c + \frac{\Delta z}{2}) + I(x_I, y_I; x_c, y_c, z_c - \frac{\Delta z}{2})] + N_{\text{bg}}\}} \\ &\quad \times \frac{1}{[I_N(x_I, y_I)]!} \end{aligned} \quad (21)$$

where the sum is evaluated over all pixels. We conclude that a PSF detects two emitters if  $\mathcal{L}(2 \text{ emitters}) > \mathcal{L}(1 \text{ emitter})$  and conclude a single emitter otherwise. The accuracy of the test is defined as the fraction of the images for which the PSF correctly detects two emitters. Since SMLM algorithms must perform joint detection and estimation simultaneously, we note that this test is a best-case estimate of discrimination performance.

The crescent PSF outperforms existing engineered PSFs optimized for 3D single-emitter localization (Figure 4A). In the three configurations considered, crescent PSF has an error rate between 5% to 29% lower than that of tetra2, the next best performing PSF. Figure 4B qualitatively explains the advantage of the crescent PSF in distinguishing between one vs. two emitters. For the same emitter positions, the difference between the one- and two-emitter images is significantly more pronounced with the crescent PSF. For the best visualization, values of  $z_c$  and  $\Delta z$  were chosen where the crescent PSF performs significantly better than tetra2.

#### 5. Conclusion

In this paper, we studied the ability of engineered PSFs to resolve closely spaced emitter pairs in 3D. Using simple mathematical reasoning, we developed a heuristic for optimizing the precision

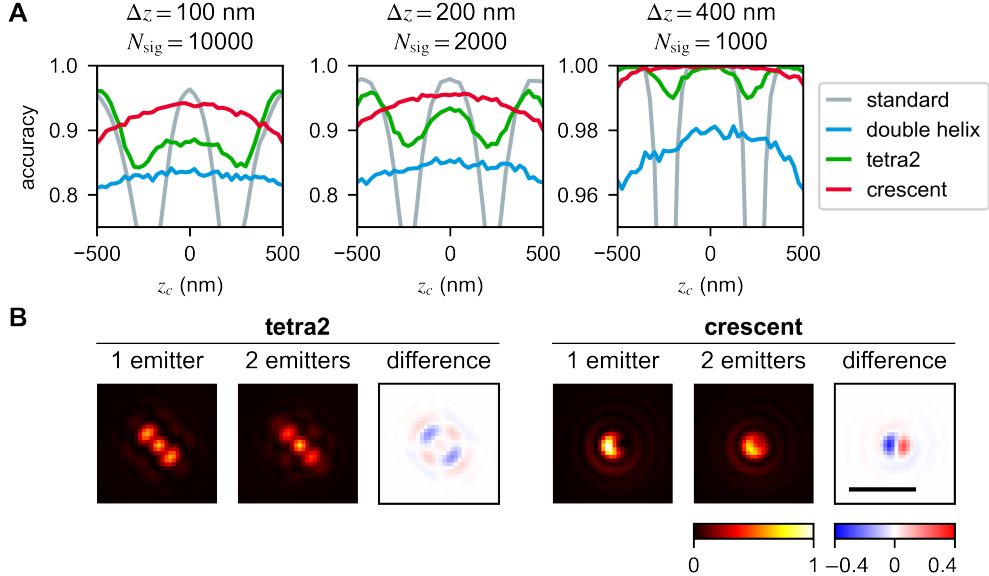


Fig. 4. (A) Accuracy of distinguishing between images containing one vs. two emitters for the standard (gray), double helix (cyan), tetrapod (tetra2, green) and crescent (red) PSFs. Accuracy values are plotted as a function of axial position  $z_c$  at three different emitter separations and signal levels. Left: separation  $\Delta z = 100$  nm and  $N_{\text{sig}} = 10000$  photons, middle:  $\Delta z = 200$  nm and  $N_{\text{sig}} = 2000$  photons, and right:  $\Delta z = 400$  nm and  $N_{\text{sig}} = 1000$  photons. At each condition, 10000 noisy images with  $N_{\text{bg}} = 10$  background photons per pixel are used to calculate accuracy. (B) Comparison of the images produced by one emitter ( $z_0 = 200$  nm) and two emitters ( $z_c = 200$  nm,  $\Delta z = 400$  nm) with a constant signal level, using the tetra2 vs. crescent PSFs. The single-emitter image is subtracted from the 2-emitter image to produce the difference image. For clarity, images are shown without Poisson noise and background noise. The color scales are in arbitrary units of intensity. Scale bar = 1  $\mu\text{m}$ .

of estimating the separation distance between two emitters, as quantified by the Cramér-Rao bound. Gradient-descent optimization of our cost function revealed a new type of PSF, called the crescent PSF, that has a simple phase mask design compared to existing corkscrew-like PSFs [14, 15, 18, 19]. We have shown that the crescent PSF performs optimally for both one- and two-emitter localization, achieving 8% superior performance for estimating the separations between emitters along the axial direction over the tetrapod PSF. It also distinguishes between the noisy images produced by one vs. two emitters with a 5-29% improvement in average error rate over the tetrapod PSF.

While the crescent PSF outperforms existing PSFs engineered for 3D single-emitter localization in many metrics, our data do not prove that is optimal for all imaging tasks. Our study primarily relies on numerical methods to explore design space and assess performance. It is notable that optimizing the cost function  $C_2$  (Equation (19)), a second-order approximation of the CRB for estimating the separation between two emitters, results consistently in two types of PSFs: one rotating, single-spot PSF and another translating, double-spot PSF. These PSFs are created by phase masks with remarkable symmetry and simple phase profiles (Figure 8). We speculate that these phase masks, which both separate Fourier space into a central disk and surrounding ring, are related to optimal axial localization of single emitters via interferometry [8]. That is, the crescent PSF's PM contains a central disk of radius  $r/r_A = 0.69$  (Figure 9), and the tetrapod-style PMs contain a central disk of radius  $r/r_A = 0.71$  (Figure 6). These sizes are very similar to that

of the annular mirror ( $r/r_A = 0.63$ ) in the interferometer in Ref. [8]. It is likely that these rings in Fourier space are ideal locations for discriminating wavefront curvature as an emitter becomes defocused. Further studies on the relationship between detection, estimation, and resolution of multiple point emitters, and the role of annular-style PMs, will be insightful for pushing 3D super-resolution imaging to its ultimate limits.

## Appendix A: Supplementary figures

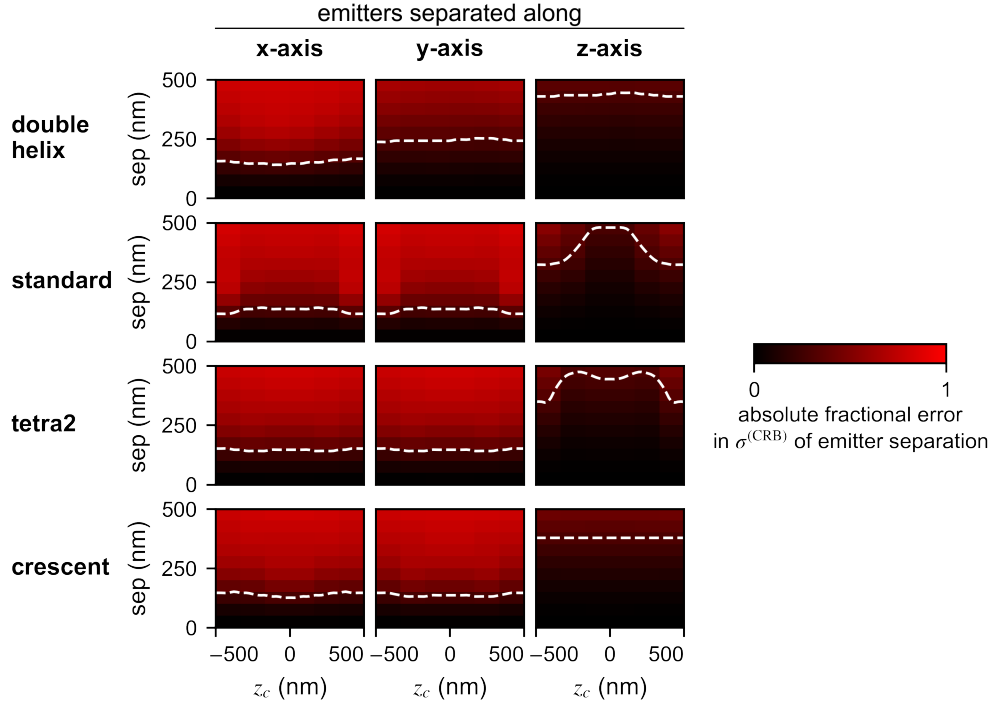


Fig. 5. Errors in approximate expressions for  $\sigma_{\Delta x}^{(\text{CRB})}$ ,  $\sigma_{\Delta y}^{(\text{CRB})}$ , and  $\sigma_{\Delta z}^{(\text{CRB})}$  i.e., Equations (12), (14) and (16), respectively, for various PSFs. Errors are plotted as a function of axial centroid  $z_c$  and appropriate emitter separation  $\Delta x$ ,  $\Delta y$ , or  $\Delta z$ . The color scale represents the absolute value of the fractional error of the expression, relative to its true value. The dashed white lines are contour lines at a fixed error of  $\pm 0.3 = \pm 30\%$ .

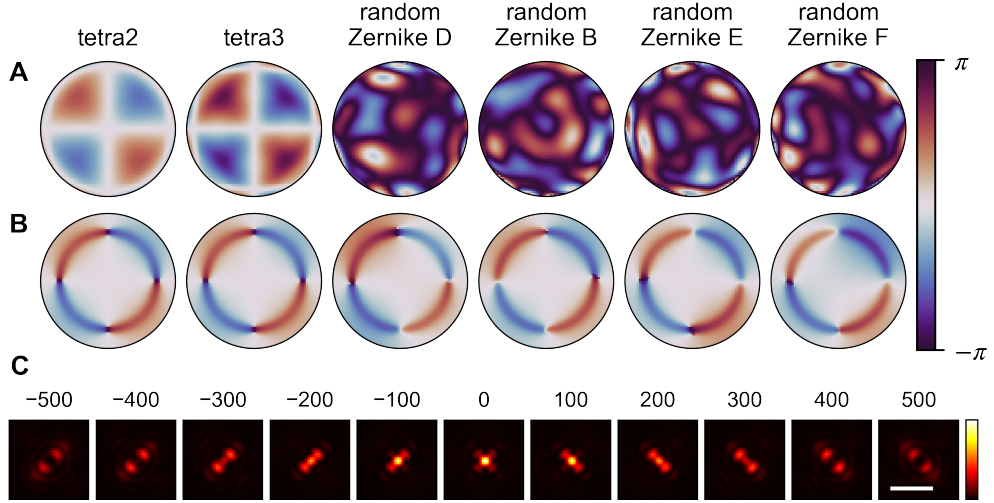


Fig. 6. Optimality and stability of a tetrapod-like PSF. (A) (B) Initial and final PMs produced by Algorithm 1 that converge to a tetrapod-like PSF. The final PMs have been normalized as described in Appendix A, Figure 8. (C) The Tetrapod-like PSF generated by the final PM from the tetra2 initial condition. The color scale represents intensity. Scale bar = 1  $\mu\text{m}$ . The PSFs generated by the other final PMs are virtually indistinguishable and are therefore not shown.

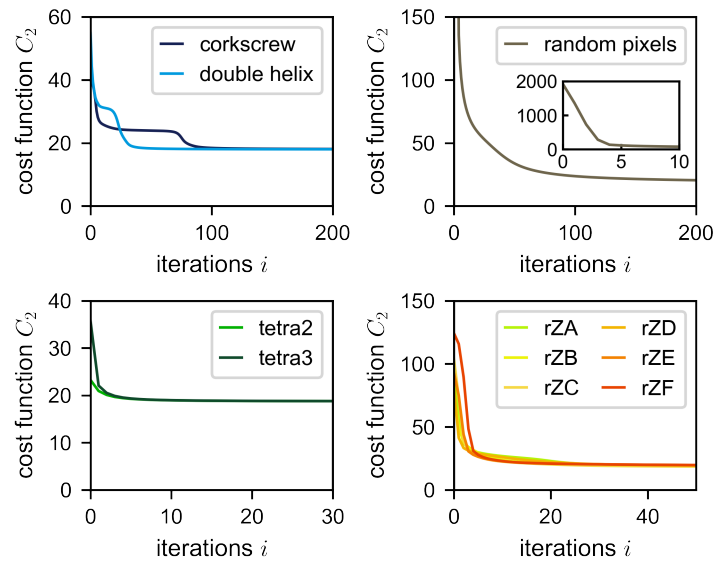


Fig. 7. Cost function  $C_2$  (Equation (19)) versus number of elapsed iterations  $i$  for all runs of Algorithm 1. Legend labels indicate the initial PM of the run; rZ = random Zernike.

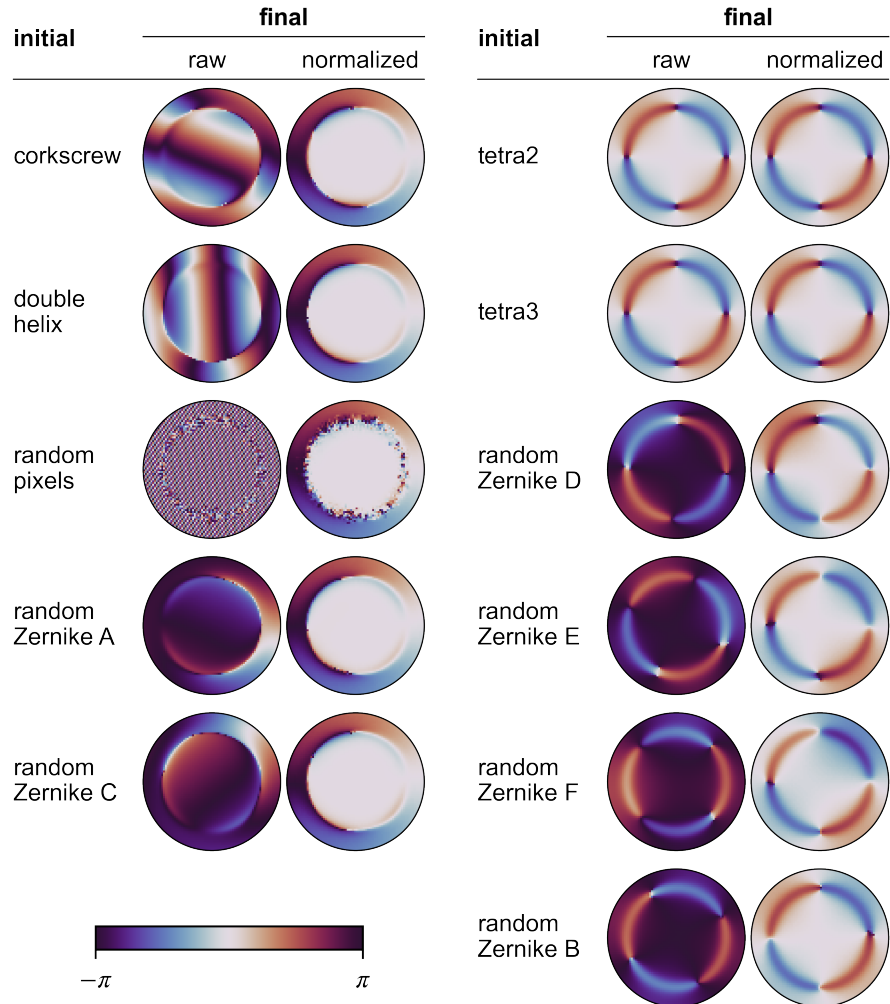


Fig. 8. Normalization of final PMs from Algorithm 1. Adding a linear function to the phase mask translates the PSF over the image space, and rotating the phase mask rotates the PSF by the same amount. These two operations can be applied to PMs without affecting their precision  $\sigma^{(\text{CRB})}$ . The exact linear functions and rotation angles are chosen by hand in order to highlight similarities between the PMs. After normalization, it is clear that there are two different classes of final PMs. The colorbar represents phase in radians.

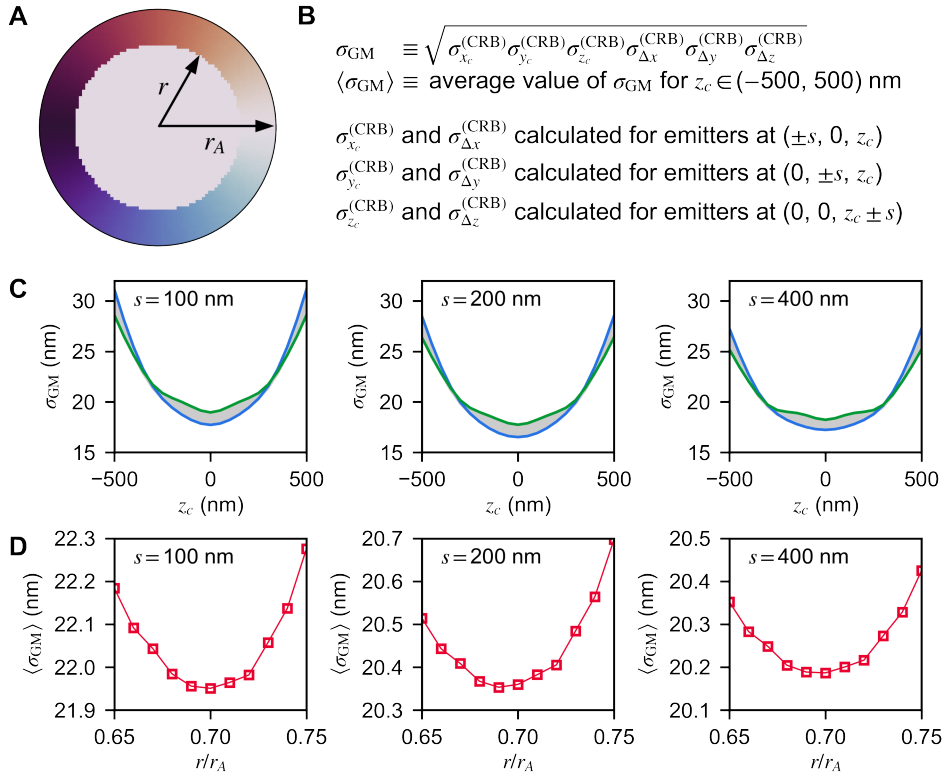


Fig. 9. Creating an idealized PM for the crescent PSF. (A) The idealized PM consists of an outer ring, where the phase shift is equal to the polar angle, and an inner circle where the phase shift is zero. Data from subsequent panels are used to determine the best value of the disk radius  $r/r_A$ . (B) Definition of quantities for subsequent panels. We seek to find the value of  $r/r_A$  that minimizes  $\langle \sigma_{GM} \rangle$ . As an overall measure of performance, this geometric mean takes into account the centroid estimation precisions as well as the separation estimation precisions for the two-emitter localization problem. (C) Mean precision  $\sigma_{GM}$  vs. centroid location  $z_c$  for  $0.65 \leq r/r_A \leq 0.75$ . The blue curve represents  $r/r_A = 0.65$ , the green curve represents  $r/r_A = 0.75$ , and curves for intermediate values of  $r/r_A$  lie in the gray region. (D) Mean precision  $\langle \sigma_{GM} \rangle$  vs.  $r/r_A$ . Based on these results, we choose  $r/r_A = 0.69$  for the idealized PM.

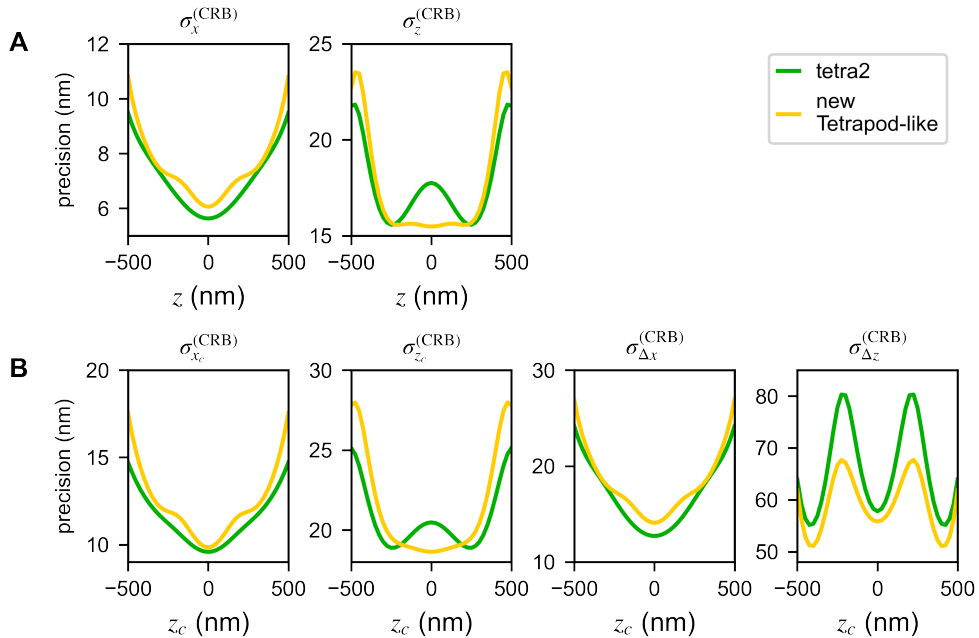


Fig. 10. Localization precision of the tetrapod (tetra2, green) and tetrapod-like (gold, Figure 6) PSFs for imaging (A) a single isolated emitter at axial position  $z$  and (B) two closely spaced emitters centered at position  $z_c$ . For the two-emitter cases, the precision of calculating lateral separation  $\sigma_{\Delta x}^{(\text{CRB})}$ , axial separation  $\sigma_{\Delta z}^{(\text{CRB})}$ , lateral centroid  $\sigma_{x_c}^{(\text{CRB})}$ , and axial centroid  $\sigma_{z_c}^{(\text{CRB})}$  are shown. The precisions are calculated for emitters that are separated laterally ( $\sigma_x^{(\text{CRB})}$  and  $\sigma_{\Delta x}^{(\text{CRB})}$ ) or axially ( $\sigma_z^{(\text{CRB})}$  and  $\sigma_{\Delta z}^{(\text{CRB})}$ ) by 200 nm. Due to symmetry,  $\sigma_y^{(\text{CRB})} = \sigma_x^{(\text{CRB})}$  and  $\sigma_{\Delta y}^{(\text{CRB})} = \sigma_{\Delta x}^{(\text{CRB})}$ . In all cases,  $N_{\text{sig}} = 1000$  photons and  $N_{\text{bg}} = 10$  photons per pixel.

**Funding.** Research reported in this publication was supported by the National Science Foundation under grant number ECCS-1653777 to M.D.L.

**Acknowledgments.** We thank W.E. Moerner and Yoav Shechtman for providing the Tetrapod phase masks. J.M.J. acknowledges support from the Caltech Summer Undergraduate Research Fellowship program.

**Disclosures.** The authors declare no conflicts of interest.

## References

1. A. von Diezmann, Y. Shechtman, and W. E. Moerner, “Three-Dimensional Localization of Single Molecules for Super-Resolution Imaging and Single-Particle Tracking,” *Chem. Rev.* **117**, 7244–7275 (2017).
2. E. Betzig, “Single Molecules, Cells, and Super-Resolution Optics (Nobel Lecture),” *Angewandte Chemie Int. Ed.* **54**, 8034–8053 (2015).
3. S. W. Hell, “Nanoscopy with Focused Light (Nobel Lecture),” *Angewandte Chemie Int. Ed.* **54**, 8054–8066 (2015).
4. W. E. Moerner, “Single-Molecule Spectroscopy, Imaging, and Photocontrol: Foundations for Super-Resolution Microscopy (Nobel Lecture),” *Angewandte Chemie Int. Ed.* **54**, 8067–8093 (2015).
5. G. Shtengel, J. A. Galbraith, C. G. Galbraith, J. Lippincott-Schwartz, J. M. Gillette, S. Manley, R. Sougrat, C. M. Waterman, P. Kanchanawong, M. W. Davidson, R. D. Fetter, and H. F. Hess, “Interferometric fluorescent super-resolution microscopy resolves 3D cellular ultrastructure,” *Proc. Natl. Acad. Sci.* **106**, 3125–3130 (2009).
6. D. Aquino, A. Schönle, C. Geisler, C. V. Middendorff, C. A. Wurm, Y. Okamura, T. Lang, S. W. Hell, and A. Egner, “Two-color nanoscopy of three-dimensional volumes by 4Pi detection of stochastically switched fluorophores,” *Nat. Methods* **8**, 353–359 (2011).
7. F. Huang, G. Sirinakis, E. S. Allgeyer, L. K. Schroeder, W. C. Duim, E. B. Kromann, T. Phan, F. E. Rivera-Molina, J. R. Myers, I. Irnov, M. Lessard, Y. Zhang, M. A. Handel, C. Jacobs-Wagner, C. P. Lusk, J. E. Rothman, D. Toomre, M. J. Booth, and J. Bewersdorf, “Ultra-High Resolution 3D Imaging of Whole Cells,” *Cell* **166**, 1028–1040 (2016).
8. M. P. Backlund, Y. Shechtman, and R. L. Walsworth, “Fundamental Precision Bounds for Three-Dimensional Optical Localization Microscopy with Poisson Statistics,” *Phys. Rev. Lett.* **121**, 023904 (2018).
9. S. Isbaner, N. Karedla, I. Kaminska, D. Ruhlandt, M. Raab, J. Bohlen, A. Chizhik, I. Gregor, P. Tinnefeld, J. Enderlein, and R. Tsukanov, “Axial Colocalization of Single Molecules with Nanometer Accuracy Using Metal-Induced Energy Transfer,” *Nano Lett.* **18**, 2616–2622 (2018). Publisher: American Chemical Society.
10. A. Ghosh, A. Sharma, A. I. Chizhik, S. Isbaner, D. Ruhlandt, R. Tsukanov, I. Gregor, N. Karedla, and J. Enderlein, “Graphene-based metal-induced energy transfer for sub-nanometre optical localization,” *Nat. Photonics* **13**, 860–865 (2019).
11. K. C. Gwosch, J. K. Pape, F. Balzarotti, P. Hoess, J. Ellenberg, J. Ries, and S. W. Hell, “MINFLUX nanoscopy delivers 3D multicolor nanometer resolution in cells,” *Nat. Methods* **17**, 217–224 (2020).
12. M. Paúr, B. Stoklasa, J. Grover, A. Krzic, L. L. Sánchez-Soto, Z. Hradil, and J. Řeháček, “Tempering Rayleigh’s curse with PSF shaping,” *Optica* **5**, 1177–1180 (2018).
13. M. Tsang, R. Nair, and X. Lu, “Quantum Theory of Superresolution for Two Incoherent Optical Point Sources,” *Phys. Rev. X* **6**, 031033 (2016).
14. E. Nehme, D. Freedman, R. Gordon, B. Ferdinand, L. E. Weiss, O. Alalouf, T. Naor, R. Orange, T. Michaeli, and Y. Shechtman, “DeepSTORM3D: dense 3D localization microscopy and PSF design by deep learning,” *Nat. Methods* **17**, 734–740 (2020).
15. E. Nehme, B. Ferdinand, L. E. Weiss, T. Naor, D. Freedman, T. Michaeli, and Y. Shechtman, “Learning optimal wavefront shaping for multi-channel imaging,” *IEEE Transactions on Pattern Analysis Mach. Intell.* **43**, 2179–2192 (2021).
16. S. R. P. Pavani, M. A. Thompson, J. S. Biteen, S. J. Lord, N. Liu, R. J. Twieg, R. Piestun, and W. E. Moerner, “Three-dimensional, single-molecule fluorescence imaging beyond the diffraction limit by using a double-helix point spread function,” *Proc. Natl. Acad. Sci. U.S.A.* **106**, 2995–2999 (2009).
17. Y. Shechtman, L. E. Weiss, A. S. Backer, S. J. Sahl, and W. E. Moerner, “Precise Three-Dimensional Scan-Free Multiple-Particle Tracking over Large Axial Ranges with Tetrapod Point Spread Functions,” *Nano Lett.* **15**, 4194–4199 (2015).
18. M. D. Lew, S. F. Lee, M. Badieirostami, and W. E. Moerner, “Corkscrew point spread function for far-field three-dimensional nanoscale localization of pointlike objects,” *Opt. Lett.* **36**, 202–204 (2011).
19. S. Prasad, “Rotating point spread function via pupil-phase engineering,” *Opt. Lett.* **38**, 585–587 (2013). Publisher: OSA.
20. S. M. Kay, *Fundamentals of Statistical Signal Processing: Estimation Theory*, vol. 1 (Prentice Hall, Upper Saddle River, NH, 1993).